Multitemporal SAR and Polarimetric SAR Optimization and Classification: Reinterpreting Temporal Coherence

Jun Ni, Carlos López-Martínez, *Senior Member, IEEE*, Zhongbo Hu, Fan Zhang, *Senior Member, IEEE*

***Abstract*—In multitemporal SAR and Polarimetric SAR (PolSAR) coherence is a capital parameter to exploit common information between temporal acquisitions. Yet, its use is limited to high coherences. This article proposes the analysis of low coherence scenarios by introducing a reinterpretation of coherence. It is demonstrated that coherence results from the product of two terms accounting for coherent and radiometric changes, respectively. For low coherences, the first term presents low values, preventing its exploitation for information retrieval. The information provided by the second term can be used in these circumstances to exploit common information. This second term is proposed, as an alternative to coherence, for information retrieval for low coherences. Besides, it is shown that polarimetry allows the temporal optimization of its values. To prove the benefits of this approach, multitemporal SAR and PolSAR data classification is considered as a tool, showing that improvements of the classification overall accuracy may range between 20% and 50%, compared to classification based on coherence.**

***Index Terms*—SAR, Coherence, Polarimetric SAR, Change Detection, Classification, Crop Monitoring**

I. Introduction

SYNTHETIC aperture radar (SAR) technology is able to provide Earth surface imagery almost independently of weather conditions and the day–night cycle, as the atmosphere is practically transparent at microwave frequencies. When considering spaceborne platforms, SAR systems can provide systematic global coverage with regular revisiting times. Combined together, these capabilities make SAR systems an important and reliable technology to provide multitemporal data series that can be employed to analyze and to characterize the different dynamical processes occurring at the Earth surface, but also to monitor human activities and their interaction with the environment. Thus, SAR systems are powerful tools to monitor the climate change and to support adaptation actions. There are many examples of current and future spaceborne SAR systems: Sentinel-1a&b (C-band), BIOMASS (P-band), NiSAR (L&S-band), ALOS (L-band), Radarsat-2 and RCM (C-band), TerraSAR-X/TanDEM-X/PAZ (X-band), GF3 (C-Band), LuTan-1a&b (L-band) or SAOCOM-1a&b. In many cases, these systems form constellations to reduce revisit times: 4-day for RCM, 6-day for Sentinel-1a&b or 8-day for SAOCOM-1a&b.

In the case of SAR systems, the first source of temporal information is the multitemporal series of the direct radar observables. For single channel SAR systems, this corresponds to the multitemporal SAR image's intensities, whereas for Polarimetric SAR (PolSAR) systems, this corresponds to the mutitemporal series of coherency or covariance matrices. For repeat pass configurations, and due to the interferometric capabilities of SAR systems, additional and complementary temporal information is captured by the complex interferometric coherence, also referred to as temporal coherence, constructed from pairs of SAR images [1], exploiting the temporal dependence between SAR images. In classical interferometry, coherence is modelled as the product of several decorrelations terms [2], in a way that these terms degrade the quality of the information that can be extracted from coherence. A group of these factors depends on the SAR system and the imaging process, such as the thermal or the geometric decorrelation terms. Ohter decorrelation terms, such as the volume decorrelation [3], depend on the scatterer characteristics. For multitemporal SAR acquisitions, coherence depends also on the temporal decorrelation term, which accounts for changes in the scatterer between acquisitions. Therefore, scenarios characterized by a low temporal coherence, for instance, long temporal baseline configurations or datasets affected by strong weather effects, prevent the extraction of temporal information from coherence. Consequently, the use of coherence is generally focused on high temporal coherence scenarios, where Polarimetric SAR Interferometry (PolInSAR) [3], [4] and Differential SAR Interferometry [5], [6] are good examples.

This paper analyzes the extraction of common temporal information from multitemporal SAR and PolSAR datasets in low temporal coherence scenarios, and establishes the relation with the temporal information extracted from direct radar observables. The basis of this study is on different previous works on coherence and change detection analysis. On the one hand, coherence has been proved to be helpful for land cover

This work was supported by the National Natural Science Foundation of China under Grant 61871413, by the China Scholarship Council under Grant 2020006880033 and by the project INTERACT $PID2020-114623RB-C32$ funded by the Spanish $MCIN/AEI/10.13039/501100011033$. (*Corresponding author: Carlos López-Martínez*).

The authors would like to thank Marco Lavalle to select the UAVSAR dataset, the European Space Agency for providing the Flevoland dataset under the AgriSAR 2009 campaign, MDA for providing the Barcelona dataset through the project SOAR-EU 6779 and the Institut Cartogràfic i Geològic de Catalunya for making public the Barcelona ground truth.

J. Ni is also with the College of Information Science & Technology, Beijing Univ. of Chemical Technology, Beijing, China, and is also with the Signal Theory & Communication Dept., Univ. Politècnica de Catalunya, Barcelona, Spain.

C. López-Martínez and Z. Hu are with the Signal Theory & Communication Dept., Univ. Politècnica de Catalunya, Barcelona, Spain.

F. Zhang is with the College of Information Science & Technology, and also with the Interdisciplinary Research Center for Artificial Intelligence, Beijing Univ. of Chemical Technology, Beijing, China.

and vegetation mapping [7]–[10], where shorter temporal baselines, leading to larger coherence values, have been shown to perform better [1]. On the other hand, polarimetry has been employed for optimized change detection [11] and crop phenological monitoring based on the optimized polarimetric contrast ratio [12]. We propose a reinterpretation of the temporal coherence, linking the previous works under a common theory, demonstrating that coherence can be separated into two terms: a first symmetric term accounting for coherent changes and a second asymmetric term accounting for radiometric changes. For low temporal coherence scenarios, the symmetric term presents low values, preventing the use of coherence. Nevertheless, the information provided by the asymmetric term can be used in these circumstances to exploit common information between SAR acquisitions. We propose the use of this information, as an alternative to coherence, for information retrieval in low temporal coherence scenarios. To prove the usefulness of this approach, we consider different classification strategies in the field of Machine Learning (ML) and Deep Learning (DL), with four different multitemporal SAR and PolSAR datasets. Classification is focused on agricultural areas as archetype of highly variable environment. As shown, the use of the information provided by the asymmetric coherence term, compared to coherence, improves the classification overall accuracy (OA) between 20% and 50%. For reference, classification results with intensities and PolSAR observables are also provided. Classification is considered in the paper as a mean to prove the benefits of the asymmetric coherence term in the analysis of low coherence scenarios, but its use can be extended to other applications.

II. Temporal Coherence

A. Temporal SAR Coherence

Given two SAR acquisitions S_1 and S_2, their coherence is

$$\rho = |\rho| e^{j\phi} = \frac{E\{S_1 S_2^*\}}{\sqrt{E\{|S_1|^2\} E\{|S_2|^2\}}} \tag{1}$$

where $E\{\cdot\}$ refers to the expectation, $|\cdot|$ is the absolute value and * is the complex conjugation. If both SAR images refer to two temporal acquisitions, (1) is referred to as repeat pass interferometric coherence or temporal coherence. In practice, the coherence is obtained by estimating the expectation $E\{\cdot\}$ by means of a speckle noise filter [13].

For temporal SAR acquisitions, assuming the absence of radiometric changes by considering the symmetrized intensity value $|S|^2 = (|S_1|^2 + |S_2|^2)/2$, (1) can be written as

$$\rho = \rho_{sym} \rho_{asym} \tag{2}$$

$$\rho_{sym} = \frac{E\{S_1 S_2^*\}}{\frac{E\{|S_1|^2 + |S_2|^2\}}{2}} \tag{3}$$

$$\rho_{asym} = \frac{\frac{E\{|S_1|^2 + |S_2|^2\}}{2}}{\sqrt{E\{|S_1|^2\} E\{|S_2|^2\}}}. \tag{4}$$

Eq. (2) decomposes coherence into two terms. The term ρ_{sym} accounts for the coherence under the symmetric assumption of no radiometric changes between SAR images, i.e., $|S_1|^2 = |S_2|^2$. Therefore, it can be decomposed into the multiplication of the classical decorrelation terms [2]

$$\rho_{sym} = \rho_{temp} \rho_{SNR} \rho_{rg} \rho_{vol} \rho_{other} \tag{5}$$

accounting respectively for the temporal, the signal-to-noise ratio, the range, the volume and other decorrelation effects. The second term of (2) ρ_{asym} accounts for the departure from the symmetric assumption, i.e., $|S_1|^2 \neq |S_2|^2$, therefore accounting for non-coherent or radiometric changes between both SAR images. This term corresponds also to the quotient of the arithmetic mean versus the geometric mean of the SAR images intensities, that according to the inequality of the arithmetic mean and the geometric mean for real non-negative $|S_1|^2$ and $|S_2|^2$, results into $\rho_{asym} \in [1, \infty)$ [14]. To understand the interpretation of ρ_{asym}, it is interesting to derive the relation with the ratio of SAR images intensities, which is often considered in change analysis of SAR data

$$\tau_{12} = \frac{E\{|S_1|^2\}}{E\{|S_2|^2\}} \tag{6}$$

where $\tau_{12} \in [0, \infty)$. It can be shown that $\rho_{asym} = (1/2)(\sqrt{\tau_{12}} + \sqrt{\tau_{12}}^{-1})$, demonstrating that ρ_{asym} can be defined in terms of τ_{12}, but the opposite is not true. The term ρ_{asym} has the advantage that its inverse follows $\rho_{asym}^{-1} \in [0, 1]$. For $\rho_{asym}^{-1} = 1$, there are no radiometric changes, i.e., $|S_1|^2 = |S_2|^2$, or equivalently, the mean and the geometric mean, see (4), are equal, whereas for $\rho_{asym}^{-1} = 0$ the radiometric change is large. Hence, ρ_{asym}^{-1} takes the role of a temporal coherence-like parameter, accounting exclusively for radiometric changes.

Eq. (2) decomposes temporal coherence into a term ρ_{sym} collecting coherent changes, and a term ρ_{asym} collecting non-coherent or radiometric changes, allowing to consider both types of changes equally. Table I shows the values of ρ considering this decomposition. The first two rows of Table I correspond to classical cases that do not need further analysis. The third and fourth rows offer an interesting point of view crucial in this study. The third row corresponds to a general case where we consider the presence of radiometric changes and maybe the presence of coherent changes. In the limit of the absence of coherent changes, which could be referred to as *high temporal coherence scenario*, ρ would account for the changes between the two SAR acquisitions. The fourth row shows that for total decorrelation, which could be referred to as *low temporal coherence scenario*, ρ is zero and it cancels the information provided by ρ_{asym}. Therefore, in a multitemporal SAR context, the common information of changes can be extracted from ρ_{asym}, also from (6), despite the coherence being low or even zero. This situation may appear, for instance, whenever ρ_{temp} is low or even zero, a common situation with multitemporal acquisitions with large temporal baselines, or when SAR acquisitions are affected by weather effects.

This analysis proposes a decomposition of the temporal coherence between two SAR acquisitions which unifies concepts previously considered separately, in essence, the analysis of radiometric changes in terms of temporal coherence. For low, or even null temporal coherence, the common information

TABLE I
ρ GIVEN THE PRESENCE OF COHERENT OR RADIOMETRIC CHANGES.

Coh. Ch.	Rad. Ch.	Coherence value
No	No	$\rho = \rho_{sym}\rho_{asym} = 1 \cdot 1 = 1$
Yes	No	$\rho = \rho_{sym}\rho_{asym} = \rho_{sym} \cdot 1 = \rho_{sym}$
No/Yes	Yes	$\rho = \rho_{sym}\rho_{asym}$ (General case)
Yes ($\rho_{sym} = 0$)	Yes	$\rho = \rho_{sym}\rho_{asym} = 0$

between SAR acquisitions can still be obtained from ρ_{asym} or the bounded coherence-like term ρ_{asym}^{-1}.

B. Temporal Polarimetric SAR Coherence

Polarimetric diversity allows the synthetic exploration of all possible polarization states. When combined with interferometric diversity, i.e., PolInSAR, polarimetry has been extensively exploited for coherence optimization [3], [15]. Nevertheless, for multitemporal acquisitions, these approaches are limited in low coherence scenarios. To overcome this limitation, Section II-A is now extended to multitemporal PolSAR data. Considering two temporal PolSAR acquisitions characterized by the coherency matrices $\mathbf{T}_{11}$ and $\mathbf{T}_{22}$, respectively, and the temporal PolInSAR matrix $\mathbf{\Omega}_{12}$, the polarimetric temporal coherence is

$$\rho = \frac{\boldsymbol{\omega}_1^H \mathbf{\Omega}_{12} \boldsymbol{\omega}_2}{\sqrt{(\boldsymbol{\omega}_1^H \mathbf{T}_{11} \boldsymbol{\omega}_1)(\boldsymbol{\omega}_2^H \mathbf{T}_{22} \boldsymbol{\omega}_2)}} \tag{7}$$

where ^{H} is the transposed complex conjugation and $\boldsymbol{\omega}_1$ and $\boldsymbol{\omega}_2$ are unitary vectors defining the polarization of the two SAR images synthesized to obtain ρ [3], [15]. Following (2), and defining the symmetric matrix $\mathbf{T} = (\mathbf{T}_{11} + \mathbf{T}_{22})/2$ [11], [16]–[19], (7) can be decomposed as

$$\rho = \frac{\boldsymbol{\omega}_1^H \mathbf{\Omega}_{12} \boldsymbol{\omega}_2}{\boldsymbol{\omega}_1^H \mathbf{T} \boldsymbol{\omega}_2} \frac{\boldsymbol{\omega}_1^H \mathbf{T} \boldsymbol{\omega}_2}{\sqrt{(\boldsymbol{\omega}_1^H \mathbf{T}_{11} \boldsymbol{\omega}_1)(\boldsymbol{\omega}_2^H \mathbf{T}_{22} \boldsymbol{\omega}_2)}} = \rho_{sym}\rho_{asym}. \tag{8}$$

Eq. (8) represents the extension of (3) and (4), respectively, to multitemporal PolSAR data, with the possibility to optimize or maximize their values as a function of $\boldsymbol{\omega}_1$ and $\boldsymbol{\omega}_2$ [11]. The interpretation of ρ_{sym} and ρ_{asym} follows Section II-A. The term ρ_{sym} accounts, in terms of PolSAR data, for the temporal coherence under the equal scattering mechanism assumption, i.e., $\mathbf{T}_{11} = \mathbf{T}_{22}$. The second term ρ_{asym} accounts for non-coherent changes between both temporal acquisitions, allowing the characterization of multitemporal PolSAR data for low coherence scenarios.

The optimization of ρ_{asym} is obtained from the Lagrange methodology

$$L = \boldsymbol{\omega}_1^H \mathbf{T} \boldsymbol{\omega}_2 - \lambda_1(\boldsymbol{\omega}_1^H \mathbf{T}_{11} \boldsymbol{\omega}_1 - C_1) - \lambda_2(\boldsymbol{\omega}_2^H \mathbf{T}_{22} \boldsymbol{\omega}_2 - C_2) \tag{9}$$

leading to the following real eigenvalue problems

$$\mathbf{T}_{11}^{-1}\mathbf{T}\mathbf{T}_{22}^{-1}\mathbf{T}\boldsymbol{\omega_1} = \nu_\rho \boldsymbol{\omega}_1 \quad \Rightarrow \quad \mathbf{A}\mathbf{U}_A = \mathbf{\Sigma}_A \mathbf{U}_A \tag{10}$$

$$\mathbf{T}_{22}^{-1}\mathbf{T}\mathbf{T}_{11}^{-1}\mathbf{T}\boldsymbol{\omega_2} = \nu_\rho \boldsymbol{\omega}_2 \quad \Rightarrow \quad \mathbf{B}\mathbf{U}_B = \mathbf{\Sigma}_B \mathbf{U}_B. \tag{11}$$

$\mathbf{A}$ and $\mathbf{B}$ are generally non-Hermitian matrices, so $\mathbf{U}_A$ and $\mathbf{U}_B$ are not expected to contain orthogonal eigenvectors. $\mathbf{\Sigma}_A$ and $\mathbf{\Sigma}_B$ are diagonal matrices containing the eigenvalues of $\mathbf{A}$ and $\mathbf{B}$, which take the form $\nu_\rho = \lambda_1 \lambda_2^*$ [3], [15]. Therefore, the optimum values of ρ_{asym} are $|\rho_{asym,opt_i}| = \sqrt{\nu_{\rho,i}}$ for $i = 1, 2, 3$. Considering (10) and (11), it can be shown that

$$\mathbf{A} = \mathbf{B} = \frac{1}{4}[\mathbf{T}_{11}^{-1}\mathbf{T}_{22} + \mathbf{T}_{22}^{-1}\mathbf{T}_{11} + 2\mathbf{I}]. \tag{12}$$

Therefore, (10) and (11) are equivalent, so $\mathbf{A}$ and $\mathbf{B}$ present the same eigenvalues, and particularly $\boldsymbol{\omega}_1 = \boldsymbol{\omega}_2$. The vector form of ρ_{asym} (8) needs to be interpreted in terms of $\boldsymbol{\omega}_1$ and $\boldsymbol{\omega}_2$. When $\boldsymbol{\omega}_1 \neq \boldsymbol{\omega}_2$, $\rho_{asym} \in \mathbb{C}$ as two different polarizations are used to form ρ_{asym}, but also it contains polarimetric coherence information. Nevertheless, for $\boldsymbol{\omega}_1 = \boldsymbol{\omega}_2$, $\rho_{asym} \in \mathbb{R}$. In this case, the same polarization is used to form ρ_{asym}, thus it contains only radiometric information. Besides, the optimum value is obtained under this assumption, i.e., $\boldsymbol{\omega}_1 = \boldsymbol{\omega}_2$.

The optimization of ρ_{asym} leads to $\boldsymbol{\omega}_1 = \boldsymbol{\omega}_2$, a condition that does not need to be imposed. Thus, we consider the following vector form of ρ_{asym} to analyze its optimum values

$$\rho_{asym} = \frac{\boldsymbol{\omega}^H \mathbf{T} \boldsymbol{\omega}}{\sqrt{(\boldsymbol{\omega}^H \mathbf{T}_{11} \boldsymbol{\omega})(\boldsymbol{\omega}^H \mathbf{T}_{22} \boldsymbol{\omega})}} \tag{13}$$

where $\rho_{asym} \in \mathbb{R}$. The maximization of (13) is reduced to find the eigenvalues of any of the three equivalent matrices in (12), that is $(1/4)[\mathbf{T}_{11}^{-1}\mathbf{T}_{22} + \mathbf{T}_{22}^{-1}\mathbf{T}_{11} + 2\mathbf{I}] = \mathbf{U}_\rho \mathbf{\Sigma}_\rho \mathbf{U}_\rho^H$, where $\mathbf{U}_\rho$ is a unitary matrix containing the eigenvectors and $\mathbf{\Sigma}_\rho$ is a diagonal matrix containing the real eigenvalues. A simple manipulation leads to

$$\mathbf{\Sigma}_\rho = \frac{1}{4}[\mathbf{U}_\rho^H \mathbf{T}_{11}^{-1}\mathbf{T}_{22}\mathbf{U}_\rho + \mathbf{U}_\rho^H \mathbf{T}_{22}^{-1}\mathbf{T}_{11}\mathbf{U}_\rho + 2\mathbf{I}]. \tag{14}$$

Eq. (14) depends on $\mathbf{T}_{11}^{-1}\mathbf{T}_{22}$ and $\mathbf{T}_{22}^{-1}\mathbf{T}_{11}$. These are related with the polarization ratio optimization problem for two temporal PolSAR acquisitions [12], [20]

$$\tau_{12} = \frac{\boldsymbol{\omega}^H \mathbf{T}_{11} \boldsymbol{\omega}}{\boldsymbol{\omega}^H \mathbf{T}_{22} \boldsymbol{\omega}} \tag{15}$$

and its inverse. The maximization of (15), or its inverse, through the Lagrange methodology

$$L = \boldsymbol{\omega}^H \mathbf{T}_{11} \boldsymbol{\omega} - \lambda(\boldsymbol{\omega}^H \mathbf{T}_{22} \boldsymbol{\omega} - C). \tag{16}$$

results in the following real eigenvalue problems

$$\mathbf{T}_{11}^{-1}\mathbf{T}_{22}\boldsymbol{\omega} = \nu_\tau \boldsymbol{\omega} \quad \Rightarrow \quad \mathbf{T}_{11}^{-1}\mathbf{T}_{22}\mathbf{U}_\tau = \mathbf{\Sigma}_\tau \mathbf{U}_\tau \tag{17}$$

$$\mathbf{T}_{22}^{-1}\mathbf{T}_{11}\boldsymbol{\omega} = \nu_\tau^{-1} \boldsymbol{\omega} \quad \Rightarrow \quad \mathbf{T}_{22}^{-1}\mathbf{T}_{11}\mathbf{U}_\tau = \mathbf{\Sigma}_\tau^{-1} \mathbf{U}_\tau. \tag{18}$$

That is, the eigenvectors in $\mathbf{U}_\tau$ diagonalize $\mathbf{T}_{11}^{-1}\mathbf{T}_{22}$ and $\mathbf{T}_{22}^{-1}\mathbf{T}_{11}$ and both forms present inverse eigenvalues. Hence, $\mathbf{\Sigma}_\tau$ and $\mathbf{U}_\tau$ contain also the generalized eigenvalues and eigenvectors, respectively, of $\mathbf{T}_{11}$ and $\mathbf{T}_{22}$. As the diagonalization operation is unique up to a permutation, $\mathbf{\Sigma}_\rho$ and $\mathbf{\Sigma}_\tau$, following (14), are related by

$$\mathbf{\Sigma}_\rho = \frac{1}{4}[\mathbf{\Sigma}_\tau + \mathbf{\Sigma}_\tau^{-1} + 2\mathbf{I}] \tag{19}$$

that after some calculations, for a particular eigenvalue is

$$\rho_{asym,i} = \frac{1}{2}(\nu_{\tau,i} + \nu_{\tau,i}^{-1}), i = 1, 2, 3 \tag{20}$$

showing that the individual terms $\rho_{asym,i}$ can be defined in terms of $\nu_{\tau,i}$, but the opposite is not true. The first consequence

of Eqs. (19) and (20) is that $\rho_{asym,i} \in [1, \infty)$ or $\rho^{-1}_{asym,i} \in [0, 1]$.

These results generalize the previous section. Thus, the optimum values of ρ_{asym}, or the temporal coherence-like terms ρ^{-1}_{asym}, as well as the temporal eigenvalues ν_τ, are proposed to characterize and to analyse multitemporal PolSAR data in terms of the temporal coherence, which is specially useful for low temporal coherence scenarios. This analysis can also be considered for dual PolSAR data as it will be shown in Section IV. Due to (20), as well as for simplicity, we will mainly assume the use of ν_τ instead of ρ_{asym}. In what it follows, we will show the usefulness of these parameters in terms of information extraction in multitemporal SAR and PolSAR data classification. We have considered the analysis of a pair of coherency matrices, so when facing the analysis of a multitemporal series of SAR acquisitions the analysis is simply extended to all possible pairs of SAR images. Finally, and with the aim of readability, ρ_{asym} and ν_τ will refer to the set of the three optimum values.

C. Generalizations

Previously, we analyzed radiometric changes in terms of the temporal coherence, in the scalar and vector forms, and we proposed the temporal eigenvalues ν_τ to analyse multitemporal PolSAR data series, specially in the case of low temporal coherence scenarios. We have shown that the optimization of ρ_{asym} is essentially equivalent to the classical polarimetric optimization problem, resulting into the temporal eigenvalues ν_τ. It is interesting to observe that these approaches extend the concept of matrix distance by decomposing it in different components. Thus, they are equivalent to:

- Geometric distance: In the cone of Hermitian positive semi-definite matrices, the geodesic distance between two matrices $\mathbf{T}_{11}$ and $\mathbf{T}_{22}$ is defined as [21], [22]

$$\delta_g(\mathbf{T}_{11}, \mathbf{T}_{22}) = \left(\sum_{i=1}^{3} log^2 \lambda_{\mathbf{T}_{11}^{-1}\mathbf{T}_{22},i} \right)^{1/2} \quad (21)$$

  where $\lambda_{\mathbf{T}_{11}^{-1}\mathbf{T}_{22},i}$ are the eigenvalues of $\mathbf{T}_{11}^{-1}\mathbf{T}_{22}$. Hence, when analysing the polarimetric ratio (15) or the vector form of ρ_{asym} (13), the geometric distance information is being considered.
- Symmetric revised Wishart dissimilarity: This dissimilarity measure assumes that $\mathbf{T}_{11}$ and $\mathbf{T}_{22}$ follow a Wishart distribution and it performs a statistical hypothesis test to evaluate if they follow the same distribution [23]

$$d_{sw}(\mathbf{T}_{11}, \mathbf{T}_{22}) = \left(tr(\mathbf{T}_{11}^{-1}\mathbf{T}_{22}) + tr(\mathbf{T}_{22}^{-1}\mathbf{T}_{11}) \right) (n_1 + n_2) \quad (22)$$

  where n_1 and n_2 are the number of pixels in the regions to calculate $\mathbf{T}_{11}$ and $\mathbf{T}_{22}$, respectively and $tr(\cdot)$ is the matrix trace. As the trace corresponds to the sum of eigenvalues, again one can see that the polarimetric ratio (15) or the vector form of ρ_{asym} (13), particularly considering (12), a distance information is being considered.

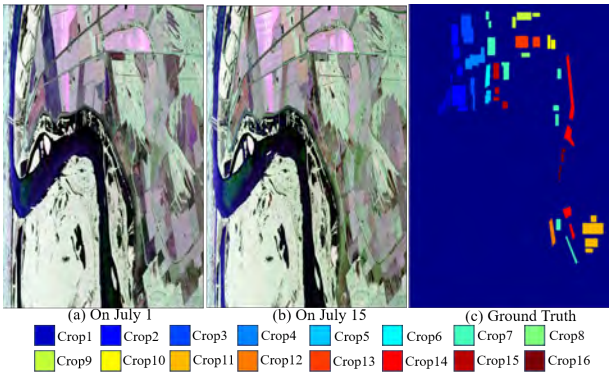

Fig. 1. UAVSAR Yucatan lake data. Pauli images on (a) July 1st, (b) July 15th and (c) Ground Truth.

- Likelihood-ratio test statistic: The statistical test if $\mathbf{T}_{11}$ and $\mathbf{T}_{22}$ belong to the same distribution is defined as [12], [24]

$$Q = 2^{6n} \frac{|\mathbf{T}_{11}|^n |\mathbf{T}_{22}|^n}{|\mathbf{T}_{11} + \mathbf{T}_{22}|^{2n}} \quad (23)$$

  where $|\cdot|$ is the matrix determinant. As shown, the term ρ^{-1}_{asym} represents the quotient between the geometric and the arithmetic means and as observed, despite the dependence on the number of averaged pixels n, ρ^{-1}_{asym} contains the likelihood-ratio test statistic information.

III. Temporal SAR and PolSAR Data

To prove the usefulness of the optimum values of ρ_{asym} and the temporal eigenvalues ν_τ for multitemporal analysis, characterization of SAR and PolSAR data, as well a for information extraction, four datasets are selected with different systems, operating frequencies, temporal spans, temporal baselines and spatial resolutions.

A. UAVSAR Yucatan lake

This is an airborne L-band multitemporal fully polarimetric dataset obtained with the UAVSAR system over Yucatan Lake wetlands site (US). It is an oxbow lake fed by the lower Mississippi river that experiences significant seasonal variability in water extent and depth, and it is a wetland of significant relevance due to its ecological importance. The dataset contains five PolSAR acquisitions collected from July 1st to September 23th, 2019, at intervals of 15, 9, 18 and 42 days, respectively. The spatial resolution is $1.67m \times 0.6m$ (Range $\times$ Azimuth) and the size of the acquisitions is 15000×9900 pixels. In this case, 9047044 pixels were manually labeled into 16 crop classes due to the absence of an external ground truth, see Table II. A total of 0.5% of the pixels are considered for training. Fig. 1 presents the Pauli images on July 1st and July 15th, together with the selected ground truth.

Fig. 2 presents the different temporal features, in logarithmic scale, characterizing the pair of PolSAR acquisitions in Fig. 1. Figs. 2-(a) to (c) detail the temporal coherences for the three polarimetric channels HH, HV and VV, where H and V indicate horizontal and vertical polarizations, respectively. In general, temporal coherences present large values as a

TABLE II
UAVSAR YUCATAN LAKE GROUND TRUTH DETAILS

Class	Type	# px.	Class	Type	# px.
1	Crop1	409499	9	Crop9	448618
2	Crop2	1441225	10	Crop10	191185
3	Crop3	977934	11	Crop11	1014105
4	Crop4	556679	12	Crop12	222613
5	Crop5	163345	13	Crop13	554334
6	Crop6	224236	14	Crop14	992410
7	Crop7	1199912	15	Crop15	422616
8	Crop8	94620	16	Crop16	133713

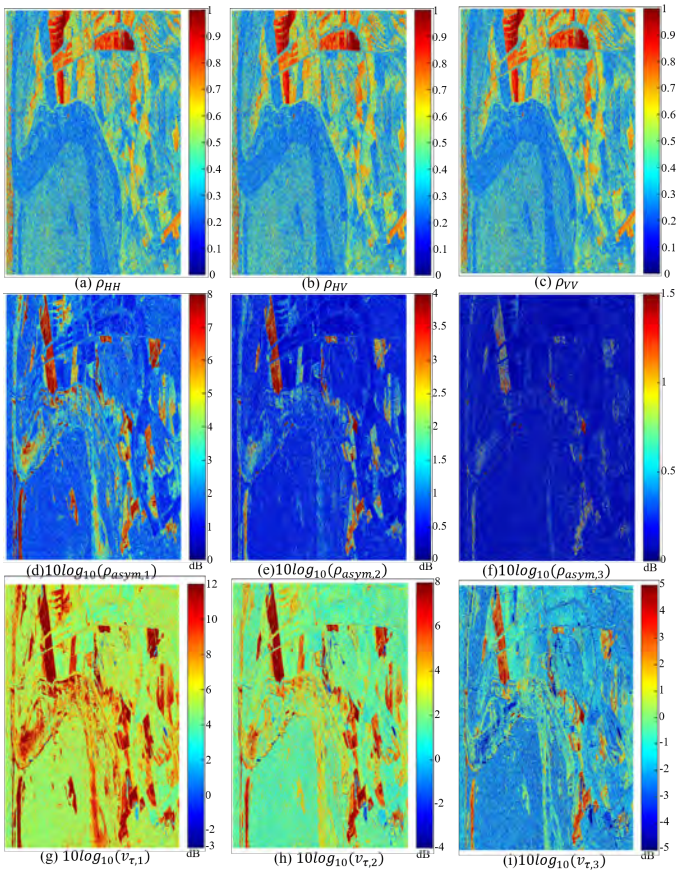

Fig. 2. Multitemporal UAVSAR Yucatan lake dataset parameters July 1st - July 15th: (a)-(c) ρ_{HH}, ρ_{HV}, ρ_{VV}; (g)-(i) $\rho_{asym,1} > \rho_{asym,2} > \rho_{asym,3} > 1$ (log scale dB); (g)-(i) $\nu_{\tau,1} > \nu_{\tau,2} > \nu_{\tau,3} > 0$ (log scale dB).

consequence of being L-band, except on water bodies. As a consequence, this dataset will be considered a *high temporal coherence scenario*. Figs. 2-(d) to (f) present the optimum values of ρ_{asym} whereas, Figs. 2-(g) to (i) show the temporal eigenvalues ν_τ. As observed, $\rho_{asym} \in [1, \infty)$, or $\rho_{asym} \in [0, \infty)$ in logarithmic scale, and $\nu_\tau \in [0, \infty)$, or $\nu_\tau \in (-\infty, \infty)$ in logarithmic scale. The first observation of Fig. 2 shows the complementary information provided by all the parameters, and in particular the values of both ρ_{asym} and ν_τ show the variation of the radiometric changes between both PolSAR acquisitions. The bottom-left area, that corresponds to the lake and the wetlands area, presents low temporal coherences, but radiometric changes can be inferred for the other two sets of parameters.

TABLE III
RADARSAT-2 FLEVOLAND GROUND TRUTH DETAILS

Class	Type	# px.	Class	Type	# px.
1	Flower bulb	156855	7	Pea	85962
2	Fruit	161879	8	Potato	1025700
3	Grass	748886	9	Spring-Wheat	71536
4	Maize	268156	10	Sugar-bee	661697
5	Miscellanea	350675	11	Winter-Wheat	1116549
6	Onion	542516	-	-	-

The temporal behavior for all the classes in Table II is detailed in Fig. 3. The first rows detail the temporal coherence values for all the temporal combinations, whereas the last rows represent the temporal eigenvalues ν_τ in logarithmic scale. Most of the classes present temporal coherence values below 0.6, indicating that the scattering features of different crops vary significantly between dates. Nevertheless, classes Crop2, Crop5, Crop11, Crop12 and Crop16 present very low coherence values for all the temporal combinations, whereas more variability is observed in ν_τ. Hence, the radiometric change information provided by ν_τ is very valuable to analyse the temporal behavior in these classes, as they are almost non distinguishable from the variation of temporal coherences.

B. Radarsat-2 Flevoland

This is a C-band multitemporal fully polarimetric dataset obtained with the spaceborne Radarsat-2 system in Flevoland (The Netherlands). This areas corresponds to a large agricultural area covered with different crops, water, and homogeneous soils. The dataset contains eight PolSAR acquisitions collected from April 14th to September 29th, 2009 in the framework of AgriSAR 2009 project. Each image is collected at an interval of 24 days. The spatial resolution is $4.73m \times 4.73m$ and the size of the acquisitions is 5300×3100 pixels. In this particular case, an external ground truth was provided comprising 5190411 pixels labelled into eleven different crops, see Table III. A total of 1% of the pixels are considered for training. Fig. 4 presents the Pauli images on April 14th and May 8th, together with the ground truth.

Temporal coherences, ρ_{asym} and the temporal eignevalues ν_τ are shown in Fig. 5. Given the 24-day temporal baseline between the PolSAR acquisitions, the temporal coherences in Figs. 5-(a) to (c) present low values, except on urban areas in the top and the bottom of the image. Thus, the different agricultural areas are almost not distinguishable in terms of temporal coherences. Thus, this dataset represents a clear *low temporal coherence scenario*. Nevertheless, a close look to the values of ρ_{asym} and ν_τ in Figs. 5-(d) to (f) and Figs. 5-(g) to (i), respectively, show an enhanced capability to distinguish the different crop areas and image details.

This enhanced capability to distinguish the different crops in terms of their temporal behavior is clearly visible in the temporal analysis of the different parameters in Fig. 6. Most of the values in the temporal coherences are centered around 0.2, therefore temporal coherence could not support the classification of different crops. By contrast, the temporal eigenvalues ν_τ show much more variability and details, making possible the differentiation of different crops, e.g., flower bulb, maize,

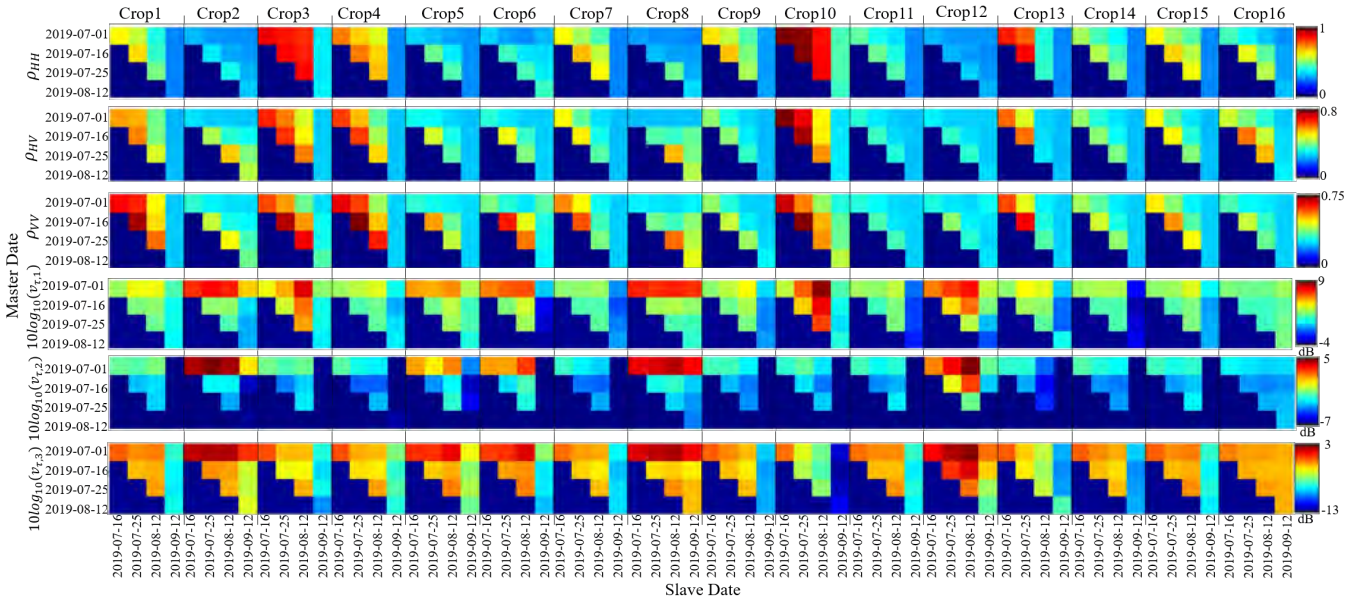

Fig. 3. Multitemporal matrices of ρ and ν_τ (log scale dB) for the UAVSAR Yucatan lake dataset.

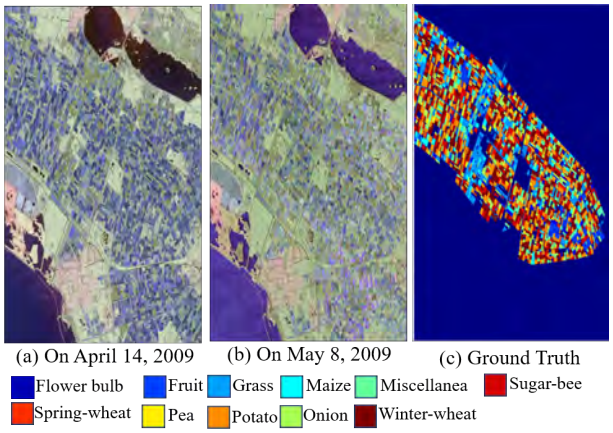

Fig. 4. Radarsat-2 Flevoland data. Pauli images on (a) April 15th, (b) May 8th and (c) Ground Truth.

miscellaneous, onion, pea, or spring-wheat, in terms of the temporal behavior of the polarimetric radiometric information.

C. Radarsat-2 Barcelona

This is a C-band fully polarimeric dataset obtained with the spaceborne Radarsat-2 system in Barcelona (Spain). This area contains the metropolitan area of the Barcelona city together with its southern region comprising a large agricultural area in the riverbanks of the Llobregat river. The dataset contains eleven PolSAR acquisitions collected from May 20th, 2010, to October 6st, 2011. The intervals of the eleven PolSAR images are 48, 24, 96, 24, 72, 48, 72, 48, 48 and 24 days. The spatial resolution is $4.73m \times 4.82m$ and the size of the acquisitions is 5726×2391 pixels. In this case, we considered a high resolution ground truth of the agricultural comprising 590890 pixels labeled into 8 crop classes, provided by the Institut Cartogràfic i Geològic de Catalunya (ICGC), see Table IV. Unlike the previous two datasets, the classes provided by ICGC comprise general land covers, or agricultural classes, and not individual types of crops, see Fig. 9. A total of 1% of the pixels are considered for training. Fig. 7 presents the Pauli images of the master acquisition and the ground truth.

TABLE IV
RADARSAT-2 BARCELONA GROUND TRUTH DETAILS

Class	Type	# px.
1	Herbaceous crops	167359
2	Orchards and cross crops	17990
3	Vineyard	3049
4	Olive	4483
5	Other woody crops	106935
6	Rotation Crops	3095
7	Coniferous forest	156529
8	Bush	131450

The multitemporal matrices of the eight land cover classes in the eleven PolSAR acquisitions are presented in Fig. 8. As observed, all temporal coherences present values below 0.6, but concentrated between 0.2 and 0.3. Some subtle seasonal effects may be inferred for some land covers, where only the cover Bush present remarkable coherence values. Nevertheless, observing the radiometric changes provided by the temporal eigenvalues ν_τ one can observe a more remarkable temporal variability. Hence, in this particular case, which could be also considered as a *low temporal coherence scenario*, coherence does not provide a real temporal behavior of the different land covers, whereas ν_τ is much more sensitive to changes, despite the low coherence values. But despite this clear difference between coherent and non-coherent or radiometric changes, it can be observed that all the land covers present very similar temporal behavior, making difficult to distinguish among them. This limitation is due to the constraints that result form the nature of the ground truth data, as it does not reflect accurate classes, but general land covers.

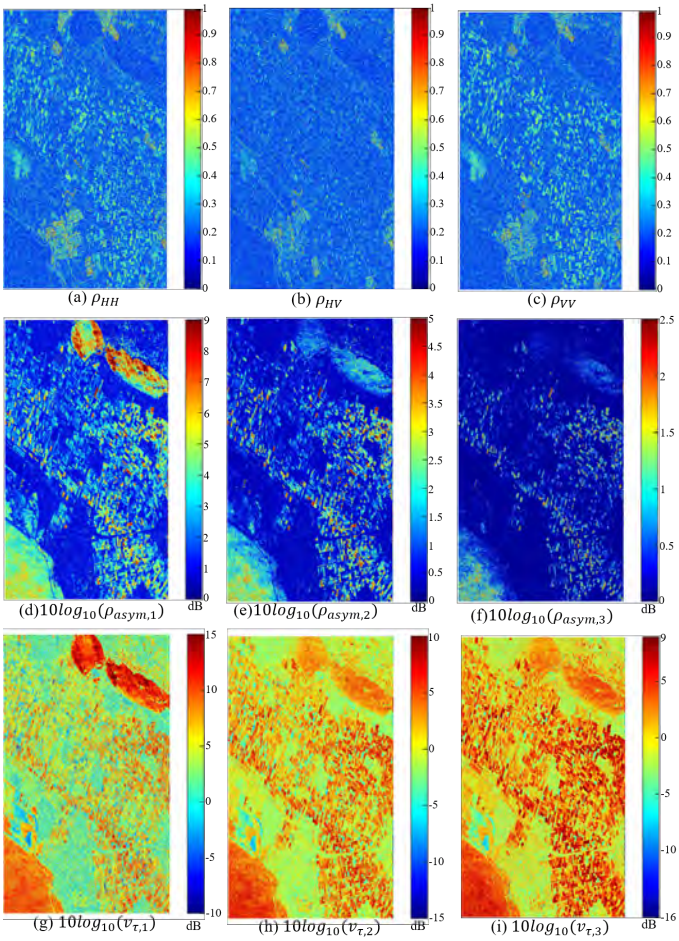

Fig. 5. Multitemporal Radarsat-2 Flevoland dataset parameters April 14th - May 8th: (a)-(c) ρ_{HH}, ρ_{HV}, ρ_{VV}; (g)-(i) $\rho_{asym,1} > \rho_{asym,2} > \rho_{asym,3} > 1$ (log scale dB); (g)-(i) $\nu_{\tau,1} > \nu_{\tau,2} > \nu_{\tau,3} > 0$ (log scale dB).

Most of these land covers correspond to vegetation, therefore they present a very similar temporal behaviour.

D. Sentinel-1 Barcelona

This is a C-band multitemporal dual-polarimetric dataset obtained with the spaceborne Sentinel-1a&b system in Barcelona (Spain). This dataset covers almost the same region as the previous datset. Nevertheless, this dataset contains 32 dual-PolSAR images collected from April 2nd to October 5th, 2018. Each image is collected at an interval of 6 days. The spatial resolution is $2.33m \times 13.95m$ and the size of the acquisitions is 2331×11061 pixels. In this case, we employed the same land cover ground truth employed in the previous dataset, but now comprising 1387587 pixels labeled into 10 classes covering crops and artificial areas, see Table V. A total of 1% of the pixels are considered for training. Fig. 10 presents the Pauli images of the master acquisition and the ground truth.

The analysis in Section II-B considered full-PolSAR data for optimization. Nevertheless, a multitemporal analysis of SAR data does not necessarily need full-PolSAR data, as the temporal eigenvalues ν_τ can be obtained form any matrix of the type $\mathbf{A}^{-1}\mathbf{B}$, independently of the matrix dimensions. Therefore, the temporal analysis in Section II-B can be extended to dual PolSAR Sentinel-1 data.

TABLE V
SENTINEL-1 BARCELONA GROUND TRUTH DETAILS

Class	Type	# px.
1	Herbaceous crops	471500
2	Orchards and cross crops	27619
3	Vineyard	20712
4	Olive	5078
5	Other woody crops	171360
6	Rotation Crops	2843
7	Bush	435313
8	Grass	82642
9	Port	143120
10	River	27400

To represent the variation of the different multitemporal features in the Sentinel-1 dataset, Fig. 11 shows the plots of the temporal coherence and the temporal eigenvalues ν_τ for the ten selected land-cover classes. As in the previous dataset, coherence is quite constant and similar among all the covers. Only the Bush and Port classes present a distinctive behavior. The former showing a seasonal effects and the later showing high coherence. The largest temporal coherence values are seen for the shortest temporal baselines, close to the diagonal. In the case of the parameters ν_τ, more radiometric changes can be observed, In herbaceous crops, the temporal features from May to July are negative, and the temporal features from July to September are positive. In Vineyard, the temporal features have obvious changes from April to May and from June to July. Finally, The temporal features in Bush have obvious changes from May to July and from August to September.

IV. EXPERIMENTAL RESULTS

A. Classification Methods

To show the usefulness and benefits of ν_τ to analyze and to characterize multitemporal SAR and PolSAR data, nine pixel-based classification methods, including two ensemble learning classifiers with two criteria and five DL networks, are implemented. In this section, classification is considered as a mean to prove the benefits of the asymmetric coherence term in the analysis of low coherence scenarios, but its use can be extended to other applications.

1) Ensemble Learning Classification Methods: Random Forest (RF) [25] and Extremely Randomized Trees (ERT) [26] have been developed for multitemporal SAR and PolSAR data classification. They are constructed with decision trees [27], and the difference among them is in the construction process. The former builds different decision trees based on the randomness of training samples, while the latter builds different decision trees based on the randomness of the input features. In the two classifiers, 500 trees are considered, and the criteria of "gini" for the Gini impurity [28] and "entropy" for the information gain [29] are employed in both classifiers, resulting into the four approaches: RF-En, RF-Gi, ERT-En, and ERT-Gi. Finally, the decision rule is the average of the classification probabilities obtained by all decision trees.

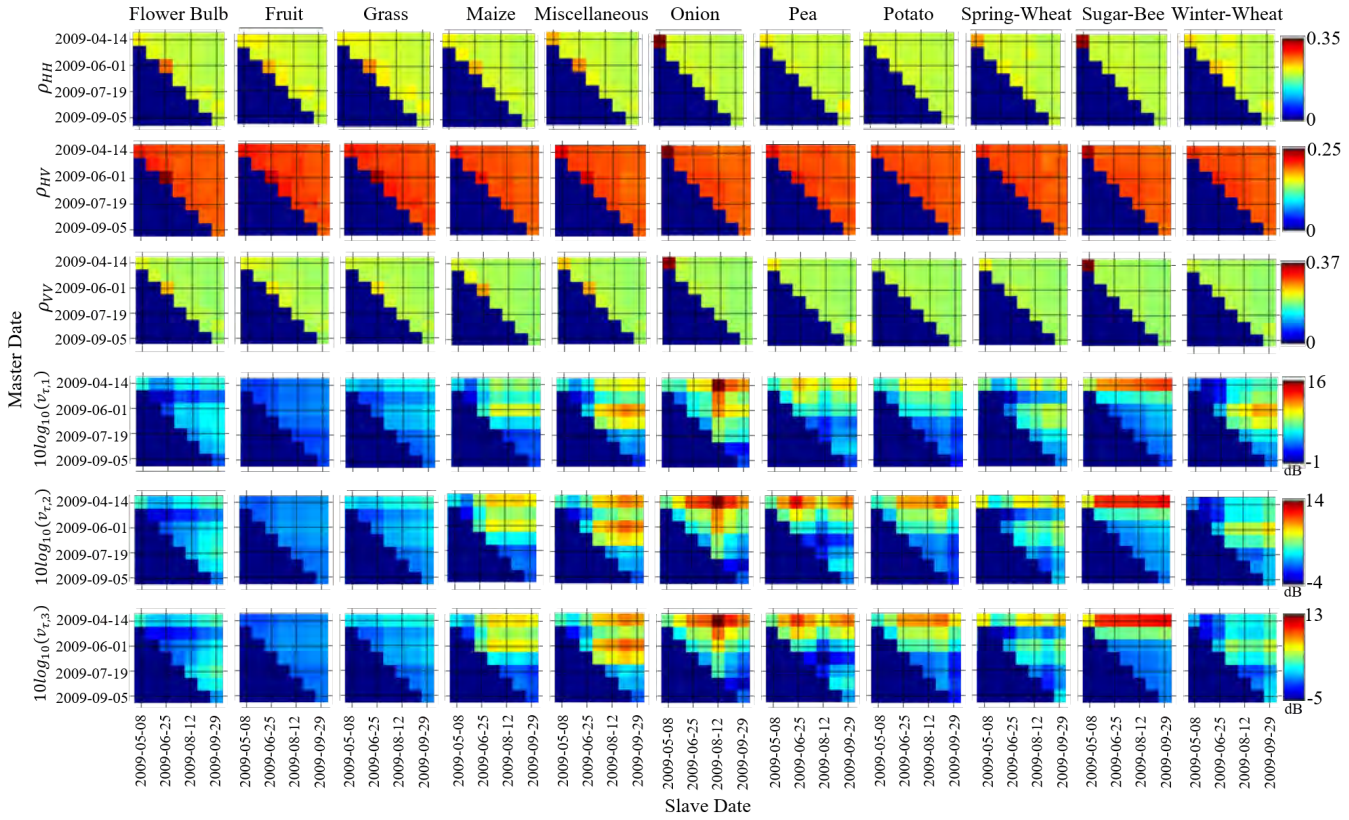

Fig. 6. Multitemporal matrices of ρ and ν_τ (log scale dB) for the Radarsat-2 Flevoland dataset.

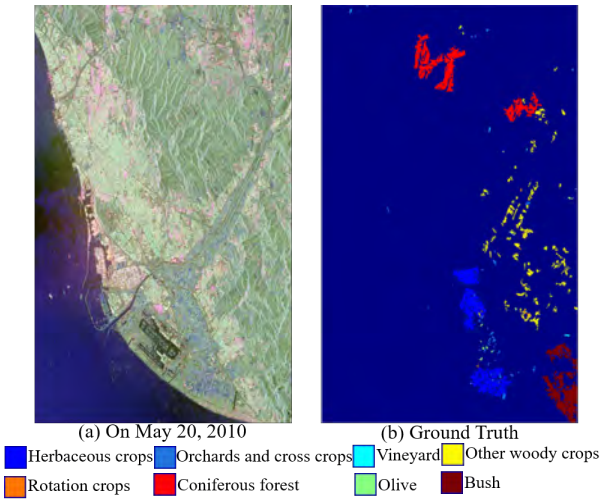

Fig. 7. Radarsat-2 Barcelona dataset.

2) Deep Learning Classification Methods: Deep neural networks (DNN) seems to be an ideal approach to perform classification due to their precise classification and independence of complex models. First, the fully connected neural network, namely FCNN, is designed to connect all features. Second, to construct the classification models from the time dimension and the feature dimension respectively, two kinds of classical deep neural networks, namely convolutional neural network (CNN) and recurrent neural network (RNN), are employed in the multi-temporal PolSAR image classification. The pixel-based time-series classifiers are designed to compare the performance of different features. All structures of these DL methods are shown in Fig. 12.

Ten dense layers, a batch Normalization (BN) layer and a dropout layer are used to construct a conventional FCNN, as shown in Fig. 12-(a). In the input layer, t is the length of time of the dataset and f is the number of polarimetric features. In the hidden layers, N is the number of hidden layer nodes in each dense layer, D is the dropout rate, and "Relu" [30] is employed for the activation function in the activation layer. In the output layer, "Softmax" is used for the classification.

In CNN, 1D-CNN [31] is designed to extract temporal features and polarimetric features respectively, as shown in Fig. 12-(b). In each convolution layer, the size of the convolution kernel K is set to 2, the stride is set to 1, and the number of the convolution kernels N is set to 512, 256, 256, 256, 256, 256, and 128. "Relu" is employed for the activation function in the activation layer after each one-dimension convolution layer. Since the polarimetric features at different times are analyzed independently in 1D-CNN, the output features extracted by one-dimension convolution layer at different times need to be expanded into one-dimensional feature vectors by Flatten.

To consider the relation between the time and the polarization dimensions in feature extraction, the deep RNN is beneficial to both time-series and polarization classification method, as shown in Fig. 12-(c). For the polarization vector of each time, there is a recursive cell corresponding to it, and

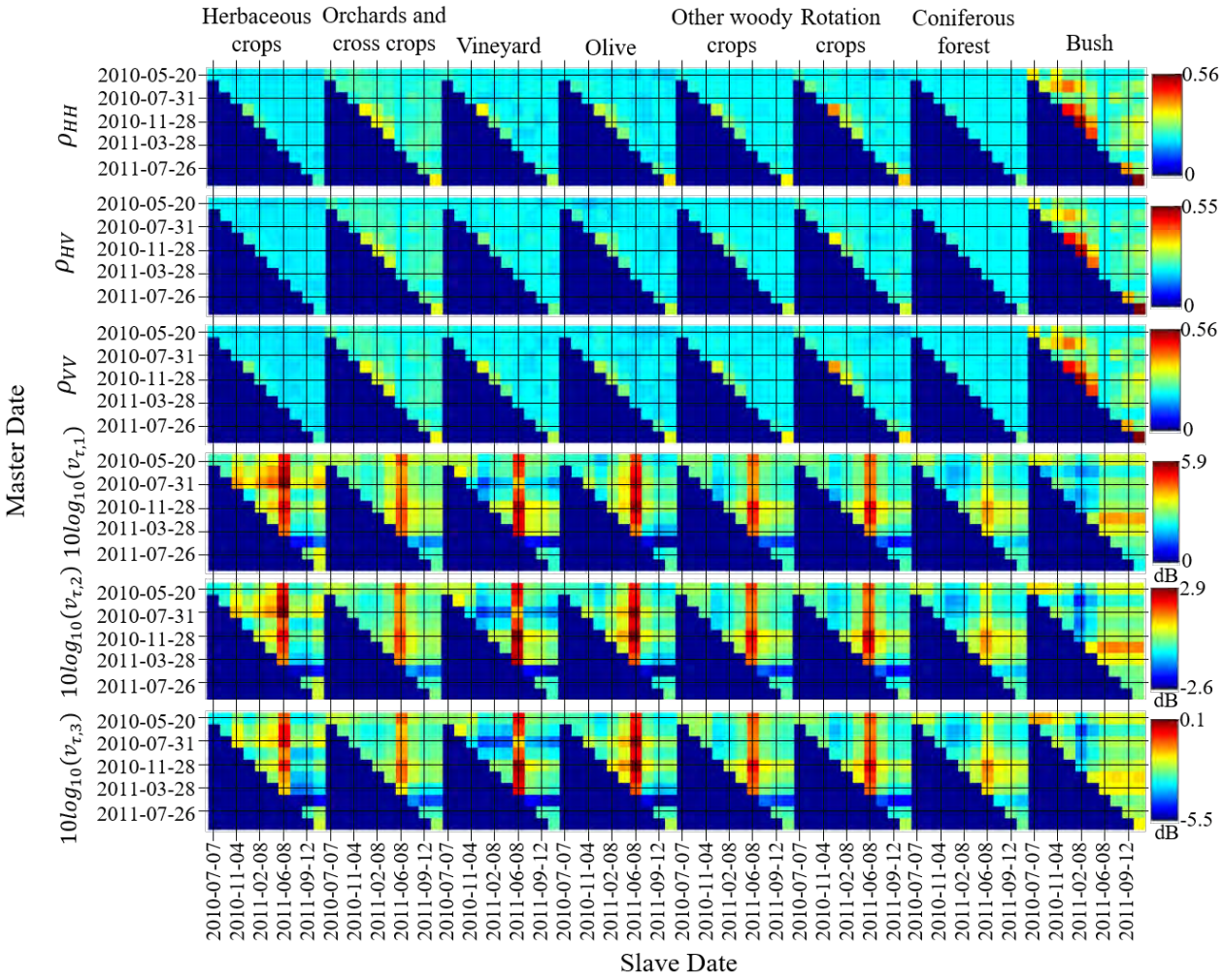

Fig. 8. Multitemporal matrices of ρ and ν_τ (log scale dB) for the Radarsat-2 Barcelona dataset.

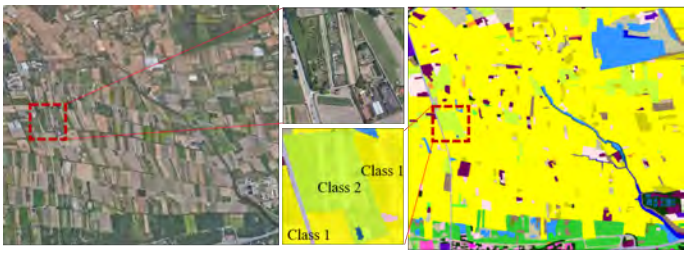

(a) Optical Image (b) Labels

Fig. 9. Barcelona ground truth detail.

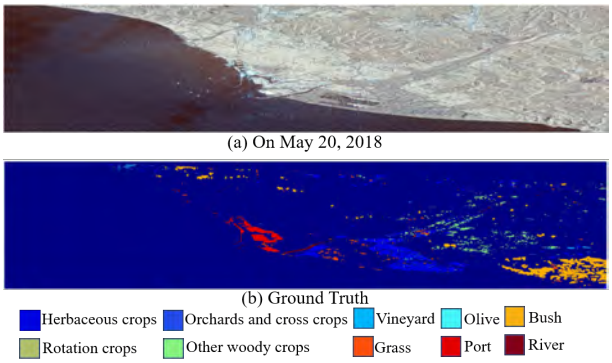

(a) On May 20, 2018

(b) Ground Truth

Fig. 10. Sentinel-1 Barcelona dataset. (a) The Pauli Image on May 20th, (b) Ground Truth.

in the time dimension, the cells in the same layer at different times establish a recursive relationship, thus forming a RNN. According to the difference of information transmission form between different cells in one layer, a variety of recursive neural network units are constructed, among which the most important structures include simple RNN [32], long short term memory (LSTM) [33], and gated recurrent unit (GRU) [34]. In this paper, simple RNN, LSTM, and GRU are designed for the temporal PolSAR image classification, and they have similar network structures as shown in Figure 12-(c). Two recursive layers are used to extract time-series and polarization features. The nodes in the two recursive layers are set to 512 and 256, respectively. Due to the wights of different cells in one recursive layer being shared, the features from the last unit of the last layer are the output of RNN, and they are input into

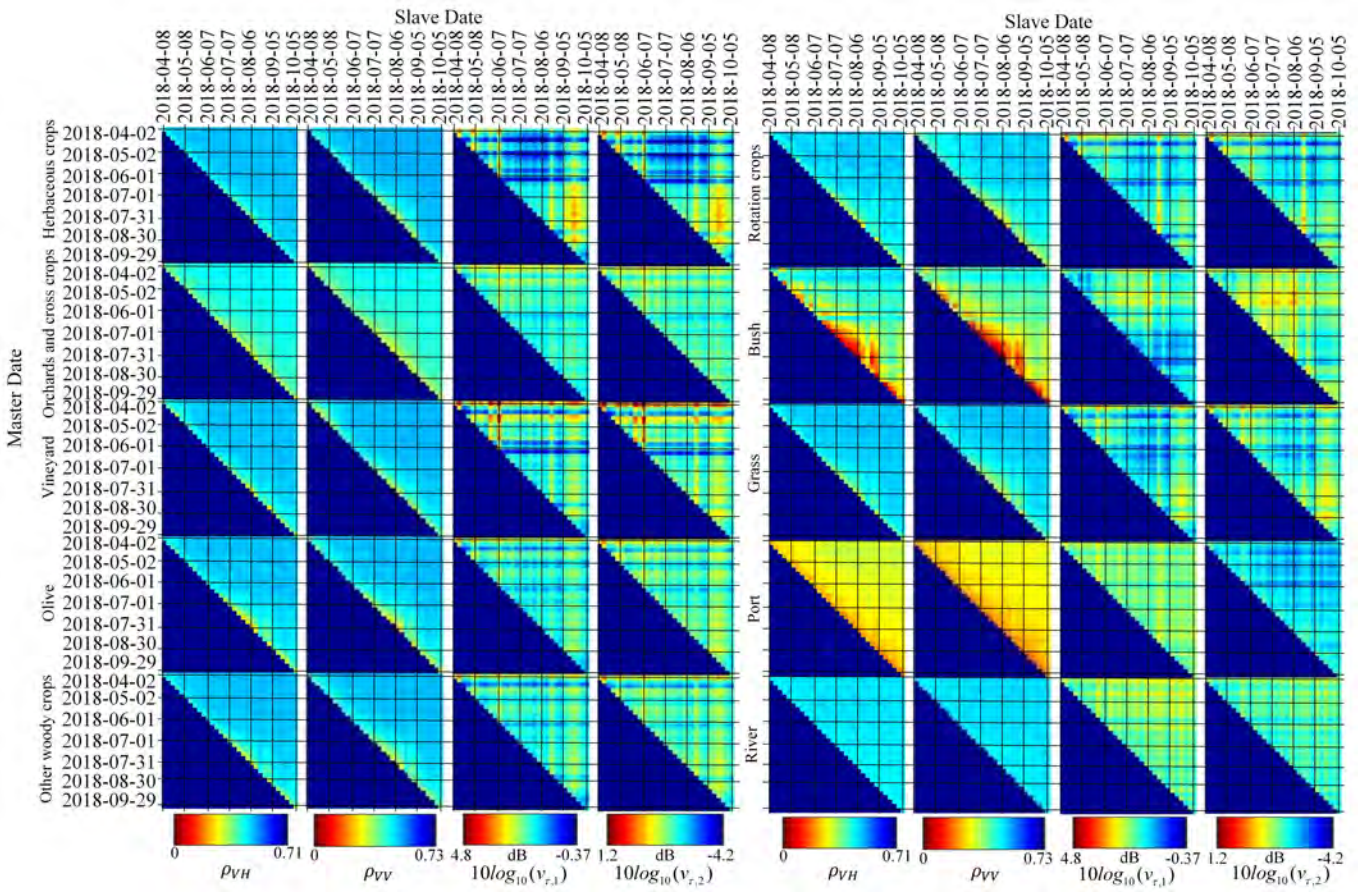

Fig. 11. Multitemporal matrices of ρ and ν_τ (log scale dB) for the Sentinel-1 Barcelona dataset.

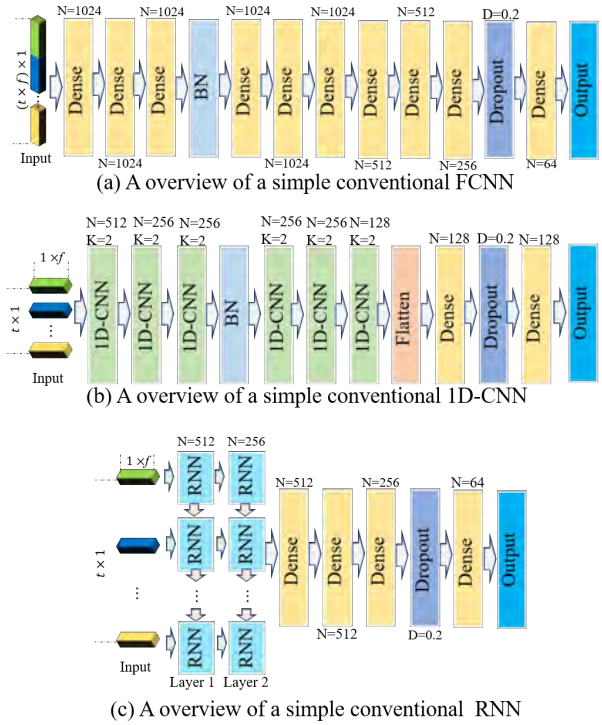

Fig. 12. Structure of the DL methods.

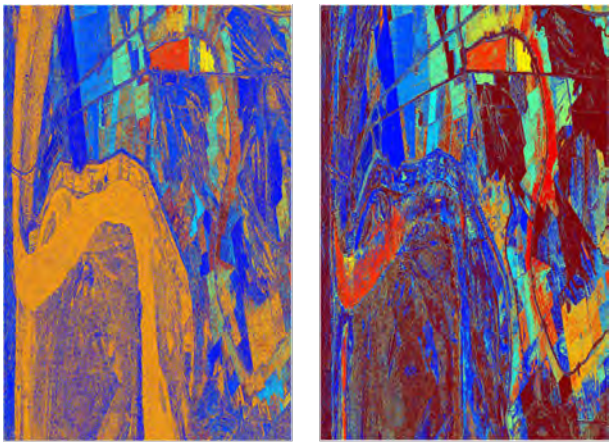

(a) GRU, Coh., 59.08% (b) GRU, Eig., 79.88%

Fig. 13. Classification maps of GRU method considering ρ (Coh.) and ν_τ (Eig.), UAVSAR Yucatan dataset.

the fully connected layers to realize classification.

B. Input Features for Classification

To demonstrate the usefulness of the temporal eigenvalues ν_τ, referred to as Eig., to characterize multitemporal SAR and PolSAR data, these are considered as input features for all the classification methods. The classification performance

TABLE VI
CLASSIFICATION RESULTS SUMMARY FOR THE EVALUATION PERFORMED WITH THE DIFFERENT METHODOLOGIES AND FEATURES SETUP

Method	No	Features	UAVSAR - Yucatan			RST-2 - Flevoland			RST-2 - Barcelona			Sentinel-1 - Barcelona		
			OA (%)	AA (%)	κ	OA (%)	AA (%)	κ	OA (%)	AA (%)	κ	OA (%)	AA (%)	κ
RF-En	1	Coh.	58.39	45.98	0.5323	32.86	17.53	0.1764	61.13	31.61	0.4783	68.38	26.8	0.5428
	2	Eig.	79.12	79.29	0.7685	81.08	67.26	0.7765	70.33	36.42	0.6056	70.57	28.56	0.5794
	3	Int.	89.61	89.74	0.885	87.78	80.15	0.8569	77.98	41.37	0.7078	75.41	37.5	0.6574
	4	T3/C2	92.67	92.9	0.9189	88.44	80.8	0.8645	77.96	41.07	0.7067	74.7	36.13	0.6451
RF-Gi	5	Coh.	58.56	45.95	0.5342	33.02	17.72	0.1792	61.3	31.79	0.4811	68.65	27.14	0.5479
	6	Eig.	79.14	79.3	0.7687	81.44	67.75	0.7808	70.46	36.51	0.6073	70.57	28.56	0.5794
	7	Int.	89.7	89.86	0.886	87.91	80.14	0.8583	77.92	41.26	0.707	75.55	37.7	0.6598
	8	T3/C2	92.67	92.81	0.9188	88.57	80.87	0.866	77.97	41.12	0.7068	74.92	36.45	0.6491
ERT-En	9	Coh.	58.2	44.47	0.5289	32.65	17.09	0.1697	60.02	30.85	0.4612	67.81	27.07	0.5332
	10	Eig.	79.18	79.21	0.7691	80.38	64.15	0.7675	70.68	36.78	0.6099	70.48	28.78	0.5756
	11	Int.	89.75	89.8	0.8866	87.84	79.09	0.8574	78.57	42.32	0.7154	75.59	37.76	0.6582
	12	T3/C2	92.46	92.55	0.9166	87.67	76.79	0.8551	77.23	41.38	0.6958	74.32	35.94	0.6372
ERT-Gi	13	Coh.	58.34	44.69	0.5307	33.06	17.4	0.1756	60.86	31.32	0.4732	68.41	27.57	0.5432
	14	Eig.	79.31	79.35	0.7705	80.62	64.57	0.7705	70.82	36.86	0.612	71.17	29.44	0.5874
	15	Int.	89.83	89.87	0.8874	87.88	79.1	0.8579	78.68	42.32	0.7168	75.92	38.14	0.6637
	16	T3/C2	92.53	92.57	0.9173	87.75	76.93	0.8561	77.71	41.62	0.7025	74.81	36.37	0.6451
FCNN	17	Coh.	57.3	47.49	0.5222	32.84	18.25	0.1839	56.71	29.44	0.4242	72.59	37.45	0.6226
	18	Eig.	78.63	79.42	0.7634	83.6	77.23	0.8083	70.13	37.24	0.6035	73.59	41.82	0.6419
	19	Int.	90.35	90.58	0.8933	89.14	84.78	0.8733	78.82	49.76	0.7215	81.45	55.16	0.7512
	20	T3/C2	84.23	84.66	0.8255	87.28	80.13	0.8513	52.8	24.08	0.3496	71.27	33.25	0.6002
CNN	21	Coh.	57.98	50.16	0.5317	33.18	18.82	0.1917	60.56	33.58	0.4794	77.49	46.52	0.6948
	22	Eig.	79.69	80.59	0.7752	82.87	75.68	0.7996	68.47	36.36	0.5827	72.77	40.93	0.6313
	23	Int.	90.65	91.8	0.8967	88.64	83.36	0.8672	76.81	44.54	0.6935	77.26	47.51	0.6951
	24	T3/C2	87.15	88.31	0.8579	88.65	83.7	0.8676	72.77	37.88	0.6389	68	31.69	0.5509
RNN	25	Coh.	58.67	48.76	0.5374	32.88	17.89	0.1794	58.62	31.27	0.4472	75.19	45.3	0.6659
	26	Eig.	80.01	80.44	0.7784	83.45	74.52	0.8059	67.97	36.32	0.5769	73.37	42.62	0.6387
	27	Int.	90.33	91.2	0.893	88.81	83.24	0.8692	78.36	47.53	0.7156	78.94	50.26	0.7173
	28	T3/C2	82.73	83.57	0.8088	89.25	85.5	0.8745	28.32	12.5	NA	36.31	12.26	0.0434
GRU	29	Coh.	59.08	49.68	0.5425	35.23	19.43	0.2106	59.34	31.07	0.4565	72.17	37.82	0.6195
	30	Eig.	79.88	80.62	0.7772	84.18	76.56	0.8148	69.09	37.54	0.591	73.98	43.45	0.6505
	31	Int.	89.84	90.46	0.8876	88.7	82.23	0.8678	77.47	45.45	0.7027	78.21	49.09	0.709
	32	T3/C2	83.88	85	0.8217	88.71	83.99	0.8683	74.37	43.98	0.6636	74.14	43.94	0.6503
LSTM	33	Coh.	58.25	49.84	0.5341	29.58	15.59	0.1352	58.1	30.36	0.4405	72.57	39.49	0.6266
	34	Eig.	79.55	80.15	0.7734	83.77	75.19	0.8099	68.27	36.83	0.5792	74.06	43.34	0.6505
	35	Int.	90.49	91.4	0.8949	88.49	83.04	0.8656	76.5	47.63	0.691	76.45	47.09	0.6831
	36	T3/C2	82.98	84.62	0.8118	87.75	76.93	0.8561	73.65	45.75	0.6531	73.45	43.32	0.6411

is compared against the one obtained by considering temporal coherences as input features too, refereed to as Coh. For completeness, the classification in terms of the intensity information of the polarimetric channels, referred to as Int., and the complete polarimetric information, in terms of the full-pol 3×3 $\mathbf{T}$ matrices for the UAVSAR and the Radarsat-2 datasets and the dual-pol 2×2 $\mathbf{C}$ covariance matrices, referred to as T3/C2, are considered as input features. When comparing the performances using the four sets of parameters it is important to highlight that the temporal eigenvalues ν_τ and the temporal coherences consider common information among pairs of SAR acquisitions, whereas the intensities and the polarimetric parameters are considering the multitemporal series of direct radar observables.

In the full-PolSAR UAVSAR and Radarsat-2 datasets, a 7×7 multi-look is considered for speckle filtering. The temporal eigenvalues ν_τ are considered in logarithmic scale, that is, $10log_{10}(\nu_\tau)$. Temporal coherences, i.e., ρ_{HH}, ρ_{HV}, and ρ_{VV} are also estimated with a 7×7 multi-look speckle noise filter. Therefore, for each of these two sets of parameters, if we consider n acquisitions, there are $3 \times n \times (n-1)/2$ features. The intensity channels are considered in logarithmic scale, i.e., $10log_{10}(|S_{HH}|)$, $10log_{10}(|S_{HV}|)$ and $10log_{10}(|S_{VV}|)$. Finally, the polarimetric information of $\mathbf{T}$, estimated also with a 7×7 multi-look window, is considered in terms of the following nine features: $\mathbf{T}_{ii}, i = 1, 2, 3$ for the diagonal elements and $\mathbb{R}\{\mathbf{T}_{ij}\}, \mathbb{I}\{\mathbf{T}_{ij}\}, i, j = 1, 2, 3, i \neq j$, for the off-diagonal elements. The Sentinel-1 dataset is considered in the same way as the full-PolSAR datasets, except that speckle is removed by means of a 4×19 multi-look window. Therefore, for n acquisitions, the set of parameters ν_τ and the temporal coherences have $2 \times n \times (n-1)/2$ input features.

C. Classification Results

The classification methods are evaluated by means of the four multitemporal datasets with the four sets of inputs features, see Table VI. It is worth to note that these classification results must be considered relative, specially when comparing results based on coherences and on temporal eigenvalues. To systematically assess the classification performances, the following parameters are being considered:

- Overall Accuracy (OA): It measures the overall classification accuracy.
- Kappa coefficient (κ): This coefficient is a quantitative evaluation of the consistency of the confusion matrix and

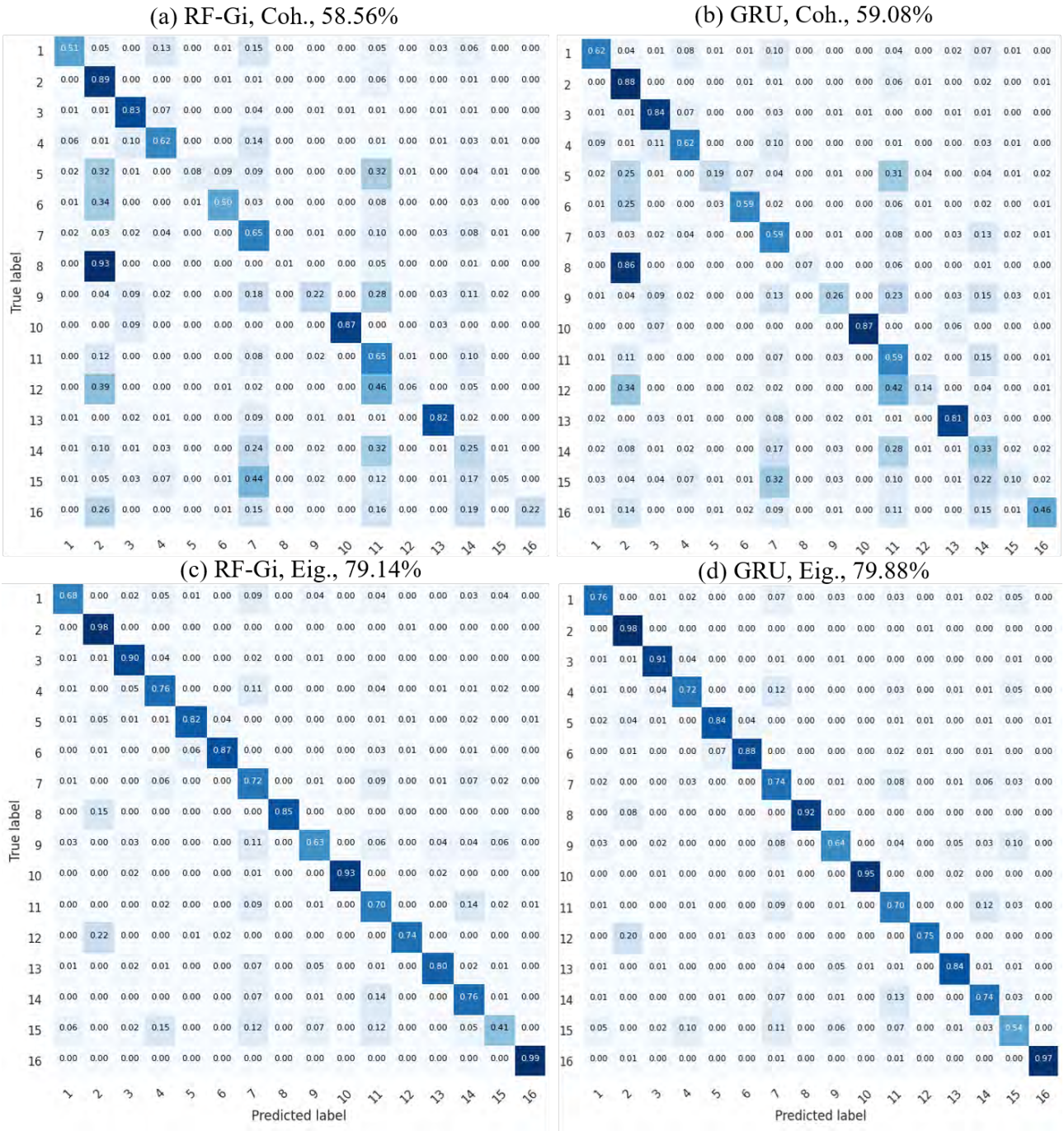

Fig. 14. Confusion matrices of the RF-Gi and GRU methods considering ρ (Coh.) and ν_τ (Eig.), UAVSAR Yucatan dataset.

it is calculated by

$$\kappa = \frac{2(TP \times TN - FN \times FP)}{(TP + FP)(FP + TN) + (TP + FN)(FN + TN)} \tag{24}$$

where TP are the true positives in the confusion matrix, FP are the false positives, TN are the true negatives, and FN are the false negatives.

- Average Accuracy (AA): It evaluates the average accuracy of each class to prevent accuracy judgment errors caused by sample imbalance, and it is calculated by

$$AA = \frac{1}{C} \sum_{i=1}^{C} recall, \tag{25}$$

where $recall = \frac{TP}{TP+FN}$ is the recall rate of each class, and C is the number of classes.

A global analysis of the classification results presented in Table VI demonstrate that when considering the common information, the proposed temporal eigenvalues ν_τ result in better classification performances that when considering coher-

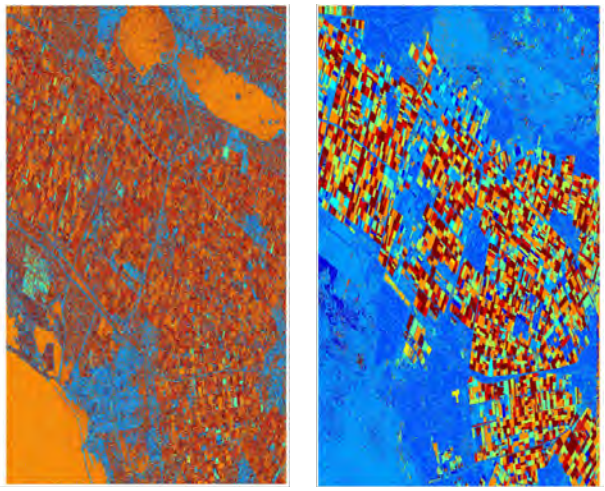

(a) GRU, Coh., 35.23% (b) GRU, Eig., 84.18%

Fig. 15. Classification maps of GRU method considering ρ (Coh.) and ν_τ (Eig.), Radarsat-2 Flevoland dataset.

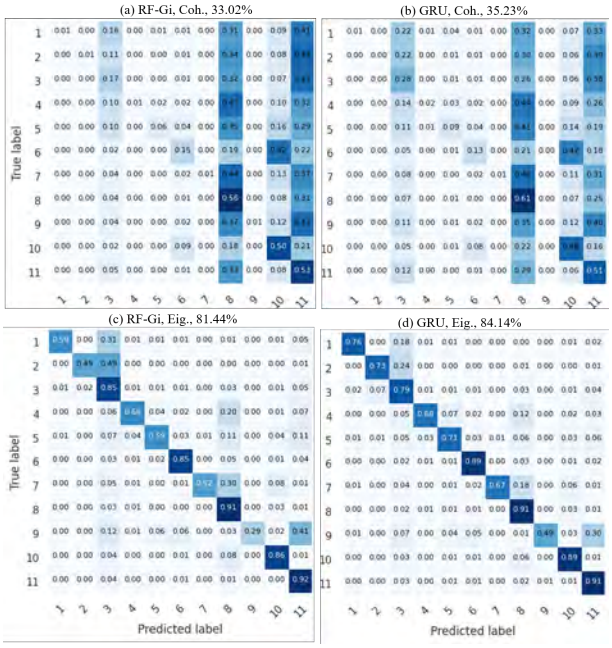

Fig. 16. Confusion matrices of the RF-Gi and GRU methods considering ρ (Coh.) and ν_τ (Eig.), Radarsat-2 Flevoland dataset.

ence information. This result is independent of the dataset or the classification methodology, proving the robustness of these parameters to exploit common multitemporal information. Classification based on the intensity parameters or the full PolSAR data result in improved classification performances. One must notice that coherences and temporal eigenvalues contain different information than intensities or full PolSAR data, and that all parameters must be seen as complementary. In the following we perform an in-depth analysis of the results in Table VI. In particular, we will present the classification maps of the GRU methodology and the confusion matrices of the RF-Gi and GRU methodologies.

In Section II, we demonstrated the relation between the optimum values of ρ_{asym} and the temporal eigenvalues ν_τ (19) and (20). Table VI shows the classification in terms of ν_τ. To compare, the OA classification results of the RF-Gi methodology based on the optimum values of ρ_{asym} is 76.5% (79.14% with ν_τ) on the UAVSAR Yucatan dataset, and 81% (81.44% with ν_τ) on the Radarsat-2 Flevoland dataset, proving the similarity of ρ_{asym} and ν_τ in classification terms.

1) UAVSAR Yucatan lake: As indicated, this dataset corresponds to a *high coherence scenario*. Therefore, the classification results must be analysed from this point of view. When considering the common information between acquisitions, in terms of temporal coherence, the OA, independently of the classification methodology, reaches a level of 60%. When considering the temporal eigenvalues ν_τ, the OA increases up to 80%. As indicated, these approaches only consider the common information between acquisitions. When considering only the acquisition themselves, in terms of intensity values or the complete full-PolSAR information, the OA reaches an average values of 85% to 90%. These results show that the temporal eigenvalues ν_τ capture better than coherence the temporal behavior of the different classes, even if these present high temporal coherence values. The classification map of GRU, extended to the whole dataset, is shown in Fig. 13, and the detailed classification information, in terms of confusion matrices of RF-Gi and GRU, is shown in Fig. 14.

In the classification results, temporal coherences of Crop2 are confused with those of Crop5, Crop6, Crop8, Crop12, and Crop16, resulting in the low classification accuracy in those categories. As observed in Fig. 3 these could be considered as low temporal coherence classes. Similarly, the temporal coherence of Crop7 is mixed with those of Crop-15, resulting in the low classification accuracy of Crop15. In the classification results of $\nu_{\tau,}$, each class is correctly classified, even if the classification accuracy of Crop9 and Crop15 are lower, and one can observe that the classification results are not significantly biased towards any other categories. Thus, the temporal eigenvalues ν_τ reflect, better than temporal coherences, the temporal information of the targets being observed.

2) Radarsat-2 Flevoland: As shown, this dataset corresponds to a *low temporal coherence scenario*. Again, the classification results must be analyzed assuming this aspect. Considering the common information, the OA considering temporal coherences reaches a level about 30%, whereas the OA reaches a level of 80% when considering the proposed temporal eigenvalues ν_τ. This result reflects the analysis presented in Section II where ν_τ were proposed to analyze the temporal behaviour of SAR images based on radiometric changes analysis, specially for *low temporal coherence scenarios*. From Fig. 6, the values of the temporal coherences for the different classes are concentrated between 0.2 and 0.3, resulting in a low OA classification performance, see Table VI. The classification maps obtained with the GRU methodology, extended to the whole dataset, are seen in Fig. 15. It must be noted that training considered only agricultural areas with available ground truth. The classification information can be observed in the confusion matrices of the RF-Gi and the GRU methodologies, see Fig. 16.

The direct observation of the confusion matrices in Fig.

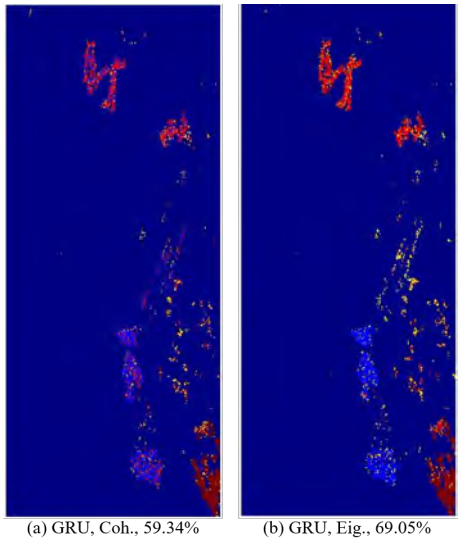

(a) GRU, Coh., 59.34% (b) GRU, Eig., 69.05%

Fig. 17. Classification maps of GRU method considering ρ (Coh.) and ν_τ (Eig.), Radarsat-2 Barcelona dataset.

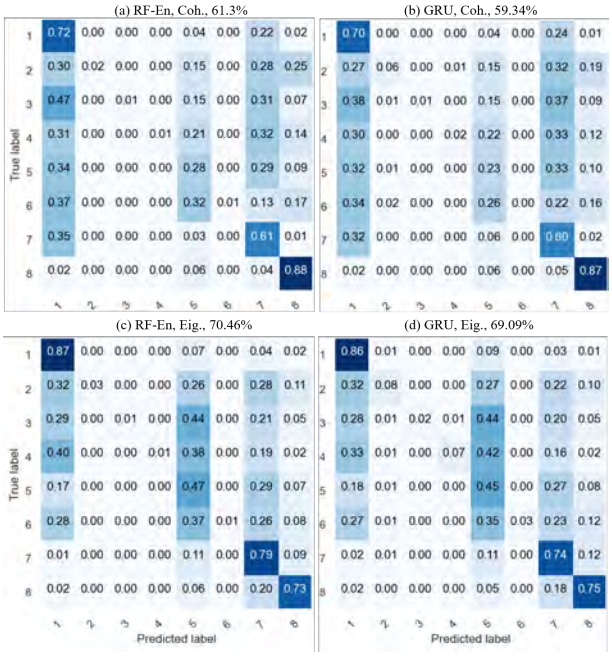

Fig. 18. Confusion matrices of the RF-Gi and GRU methods considering ρ (Coh.) and ν_τ (Eig.), Radarsat-2 Barcelona dataset.

16 clearly demonstrates the poor classification performance offered by the temporal coherence parameters, whereas the temporal eigenvalues ν_τ are able to capture all the classes. In essence, when considering the temporal coherence, the classification methodologies are only able to recognise class 8, class 10 and class 11. This limitation could be explained by the fact that almost all the classes present very low coherence values, so the classifiers map them in a limited number of classes. Nevertheless, despite the low temporal coherence values, the common temporal information exploited in terms of ν_τ is able to capture all the classes differently. Besides the κ values are large, about 0.8, indicating a high consistency of the confusion matrices. However, there are some confusions between class 2 and class 3, and between class 9 and class 11.

As indicated in Section II, we proposed the exploitation of the common temporal information in terms ν_τ for low temporal coherence scenarios. These parameters are much more sensitive than coherence to the target's temporal dynamics. But this better performance, as shown with the UAVSAR dataset, is kept also on high temporal coherence scenarios.

3) Radarsat-2 Barcelona: The previous datasets have demonstrated the capability of $\nu_{\tau,}$ to capture accurately the temporal dynamics of different types of targets, improving the classification performances with respect to use coherences as input features. One key aspect is the availability of an accurate ground truth to train the classification methodologies. As shown in Section III-C, for this dataset we considered general land cover classes. For example, the scattering features of herbaceous crops can be complex and may include different types of crops or plants. Under these circumstances, the ensemble learning classification methods are more robust than the DL methods. Therefore, the classification performance of RF-En, RF-Gi, ERT-En, and ERT-Gi is better than that of DL methods. The classification maps with GRU can be shown in Fig. 17. In this case, the classification is not extended to the whole dataset as the training considered only agricultural areas. The detailed classification information of confusion matrices with RF-En and GRU are shown in Fig. 18.

Even, under these difficult conditions, the use of ν_τ to capture the temporal behavior of the different classes, outperforms coherence by an average of 10%. This improvement is reflected in the confusion matrices of Fig. 18.

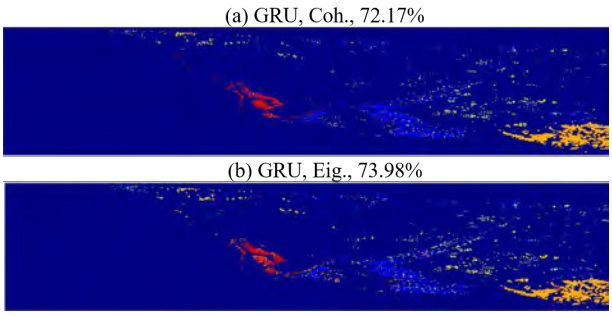

Fig. 19. Classification maps of GRU method considering ρ (Coh.) and ν_τ (Eig.), Sentinel-1 Barcelona dataset.

4) Sentinel-1 Barcelona: Compared with the previous datasets, the multitemporal dataset from Sentinel-1a&b has shorter revisit time (6 days), so the coherence of each category in Fig. 11 is larger, which can reach more than 0.7. Thus, OA of the classifiers with eigenvalue and coherence can get different classification accuracy, and overall, temporal eigenvalues perform better than coherence. In addition, insufficiently fine-grained labels, offered by ICGC, interfere with the classification performance of the classifier. The classification maps with GRU can be shown in Fig. 19. The detailed classification information of confusion matrices with RF-En and GRU is shown in Fig. 20. As in the previous dataset, the classification

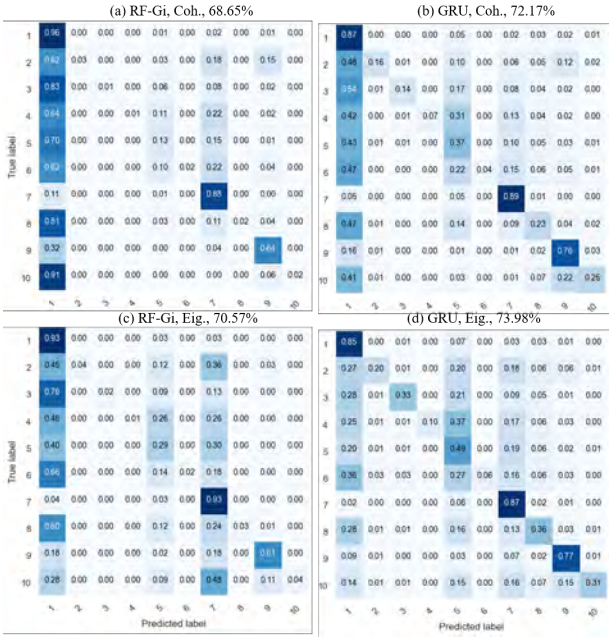

Fig. 20. TConfusion matrices of the RF-Gi and GRU methods considering ρ (Coh.) and ν_T (Eig.), Sentinel-1 - Barcelona dataset.

is not extended to the whole dataset. Classification results based on coherence are in line with [1].

In terms of classification performance, the DL classifiers with coherence can extract more features to improve it, and OA of each DL method can be improved by more than 4%. However, eigenvalues show superior classification performance in DL methods and integrated learning methods, and OA can reach more than 70%. In each category, the temporal features of class 1 and other classes are confused, so that the classifiers cannot distinguish other categories well. Compared to coherence, eigenvalues have an advantage in distinguishing class 1 versus class 5, class 7 and class 9.

V. Conclusions

A new interpretation of the temporal coherence for multitemporal SAR and PolSAR data is proposed. It is shown that the temporal coherence can be decomposed into two terms. The first symmetric coherence term accounts for coherent changes under the symmetric assumption of no radiometric changes. The second coherence asymmetric term considers non-coherent or radiometric changes. This decomposition is useful as it relates both types of changes, showing that common information between SAR acquisitions can still be extracted in low temporal coherence scenarios. First, the study is performed for single-channel multitemporal SAR data, showing that the asymmetric coherence term is related to the intensity ratio. It is important to indicate that this analysis is also valid and can be generalized for any type of SAR diversity, leading to pairs of correlated SAR images. Second, the study is extended to multitemporal PolSAR data, where polarimetric diversity allows the optimization of the asymmetric coherence term, extending the ideas of PolInSAR coherence optimization to multitemporal data. It is demonstrated that the optimum asymmetric coherence parameters are related to the optimum values of the polarimetric ratio. In addition, we show that the optimum values of the asymmetric coherence term or the polarimetric ratio are closely related to the ideas of matrix distance. As a consequence, we propose the use of the optimum values of the asymmetric coherence term or the equivalent optimum values of the polarimetric ratio to extract information for multitemporal SAR or PolSAR data, specially in low temporal coherence scenarios.

The usefulness of these parameters for multitemporal SAR or PolSAR data exploitation and interpretation is demonstrated on four different datasets by means of machine and DL classification techniques. The four datasets cover airborne versus spaceborne, L-band versus C-band, different temporal spans and different temporal baselines and spatial resolutions. The classification methodologies cover nine different techniques. In all the cases, the use of the optimum values of the asymmetric coherence term or the equivalent optimum values of the polarimetric ratio outperforms classification accuracy if compared to the use of temporal coherence as input features. In low temporal coherence scenarios improvements of 50% in the classification overall accuracy are achieved, whereas for high coherence scenarios, the improvement is about 20%. These results demonstrate the robustness of the proposed optimum values of the asymmetric coherence term or the equivalent optimum values of the polarimetric ratio to exploit multitemporal SAR and PolSAR data. Hence, we consider that the use of these parameters can be beneficial in other applications of multitemporal SAR and PolSAR data.

When considering ML or DL for remote sensing, it is argued that physical knowledge must be incorporated to reduce the need for large amounts of data, to constrain solutions to physical solutions or uncertainty reduction. As we show, one way to introduce this physical knowledge, specially in terms of remote sensing systems, is to produce physically and system relevant parameters, as the ones we proposed here. The optimum use of the information provided by the remote sensing systems is not possible without their in-depth knowledge. Therefore, we vindicate the role of remote sensing scientists and systems engineers in the era of big Earth data.

References

[1] A. W. Jacob, F. Vicente-Guijalba, C. Lopez-Martinez, J. M. Lopez-Sanchez, M. Litzinger, H. Kristen, A. Mestre-Quereda, D. Ziółkowski, M. Lavalle, C. Notarnicola, *et al.*, "Sentinel-1 InSAR coherence for land cover mapping: A comparison of multiple feature-based classifiers," *IEEE J-STARS*, vol. 13, pp. 535–552, 2020.

[2] H. Zebker and J. Villasenor, "Decorrelation in interferometric radar echoes," *IEEE Trans. Geosci. Remote Sens.*, vol. 30, pp. 950–959, Sep 1992.

[3] S. R. Cloude and K. P. Papathanassiou, "Polarimetric SAR interferometry," *IEEE Trans. Geosci. Remote Sens.*, vol. 36, pp. 1551–1565, Sept. 1998.

[4] C. López-Martínez and K. Papathanassiou, "Cancellation of scattering mechanisms in PolInSAR: Application to underlying topography estimation," *IEEE Trans. Geosci. Remote Sens.*, vol. 51, pp. 953 –965, feb. 2013.

[5] P. Berardino, G. Fornaro, R. Lanari, and E. Sansosti, "A new algorithm for surface deformation monitoring based on small baseline differential SAR interferograms," *IEEE Trans. Geosci. Remote. Sens.*, vol. 40, no. 11, pp. 2375–2383, 2002.

[6] R. Iglesias, J. J. Mallorquí, D. Monells, C. López-Martínez, X. Fàbregas, A. Aguasca, J. A. Gili, and J. Corominas, "PSI deformation map retrieval by means of temporal sublook coherence on reduced sets of SAR images," *Remote Sensing*, vol. 7, pp. 530–563, Jan. 2015.

[7] T. Strozzi, P. B. Dammert, U. Wegmuller, J.-M. Martinez, J. I. Askne, A. Beaudoin, and N. Hallikainen, "Landuse mapping with ERS SAR interferometry," *IEEE Trans. Geosci. Remote. Sens.*, vol. 38, no. 2, pp. 766–775, 2000.

[8] M. E. Engdahl and J. M. Hyyppa, "Land-cover classification using multitemporal ERS-1/2 InSAR data," *IEEE Trans. Geosci. Remote. Sens.*, vol. 41, no. 7, pp. 1620–1628, 2003.

[9] M. Santoro, J. I. Askne, U. Wegmuller, and C. L. Werner, "Observations, modeling, and applications of ERS-ENVISAT coherence over land surfaces," *IEEE Trans. Geosci. Remote. Sens.*, vol. 45, no. 8, pp. 2600–2611, 2007.

[10] N. Joshi, E. T. Mitchard, N. Woo, J. Torres, J. Moll-Rocek, A. Ehammer, M. Collins, M. R. Jepsen, and R. Fensholt, "Mapping dynamics of deforestation and forest degradation in tropical forests using radar satellite data," *Environ. Res. Lett.*, vol. 10, no. 3, p. 034014, 2015.

[11] A. Marino and I. Hajnsek, "A change detector based on an optimization with polarimetric SAR imagery," *IEEE Trans. Geosci. Remote. Sens.*, vol. 52, no. 8, pp. 4781–4798, 2013.

[12] A. Alonso González, C. López Martínez, K. Papathanassiou, and I. Hajnsek, "Polarimetric SAR time series change analysis over agricultural areas," *IEEE Trans. Geosci. Remote. Sens.*, vol. 58, no. 10, pp. 7317–7330, 2020.

[13] S. Foucher and C. López-Martínez, "Analysis, evaluation, and comparison of polarimetric SAR speckle filtering techniques," *IEEE Trans. Image Process.*, vol. 23, pp. 1751–1764, April 2014.

[14] D. G. Hoffman, *Packing Problems and Inequalities*. Boston, MA: Springer US, 1981.

[15] J. Lee and E. Pottier, *Polarimetric Radar Imaging: From Basics to Applications*. Optical Science and Engineering, CRC Press, 2017.

[16] L. Ferro-Famil, M. Neumann, and C. López-Martínez, "Analysis of natural scenes using polarimetric and interferometric SAR data statistics in particular configurations," in *Proc. International Geoscience and Remote Sensing Symposium IGARSS*, (Boston (MA), USA), July 2008.

[17] M. Tabb, J. Orrey, T. Flynn, and R. Carande, "Phase diversity: a decomposition for vegetation parameter estimation using polarimetric SAR interferometry," in *EUSAR*, June 2002.

[18] E. Colin, C. Titin-Schnaider, and W. Tabbara, "An interferometric coherence optimization method in radar polarimetry for high-resolution imagery," *IEEE Trans. Geosci. Remote. Sens.*, vol. 44, no. 1, pp. 167–175, 2006.

[19] M. Neumann, L. Ferro-Famil, and A. Reigber, "Multibaseline polarimetric SAR interferometry coherence optimization," *IEEE Geosci. Remote. Sens. Lett.*, vol. 5, pp. 93 –97, jan. 2008.

[20] A. Kostinski and W. Boerner, "On the polarimetric contrast optimization," *IEEE Trans. Antennas Propag.*, vol. 35, pp. 988 – 991, aug 1987.

[21] S. Smith, "Covariance, subspace, and intrinsic cramer-rao bounds," *IEEE Trans. Signal Process.*, vol. 53, pp. 1610–1630, May 2005.

[22] A. Alonso-Gonzalez, S. Valero, J. Chanussot, C. López-Martínez, and P. Salembier, "Processing multidimensional SAR and hyperspectral images with binary partition tree," *Proc. IEEE*, vol. 101, pp. 723–747, March 2013.

[23] A. Alonso-Gonzalez, C. López-Martínez, and P. Salembier, "Filtering and segmentation of polarimetric SAR data based on binary partition trees," *IEEE Trans. Geosci. Remote Sens.*, vol. 50, pp. 593 –605, feb. 2012.

[24] K. Conradsen, A. Nielsen, J. Schou, and H. Skriver, "A test statistic in the complex wishart distribution and its application to change detection in polarimetric SAR data," *IEEE Trans. Geosci. Remote. Sens.*, vol. 41, pp. 4–19, Jan 2003.

[25] L. Breiman, "Random forests," *Machine learning*, vol. 45, no. 1, pp. 5–32, 2001.

[26] P. Geurts, D. Ernst, and L. Wehenkel, "Extremely randomized trees," *Machine learning*, vol. 63, no. 1, pp. 3–42, 2006.

[27] J. R. Quinlan, "Induction of decision trees," *Machine learning*, vol. 1, no. 1, pp. 81–106, 1986.

[28] L. E. Raileanu and K. Stoffel, "Theoretical comparison between the gini index and information gain criteria," *Annals of Mathematics and Artificial Intelligence*, vol. 41, no. 1, pp. 77–93, 2004.

[29] T. Maszczyk and W. Duch, "Comparison of shannon, Renyi and Tsallis entropy used in decision trees," in *International Conference on Artificial Intelligence and Soft Computing*, pp. 643–651, Springer, 2008.

[30] Y. Li and Y. Yuan, "Convergence analysis of two-layer neural networks with relu activation," *Adv. Neural Inf. Process. Syst.*, vol. 30, 2017.

[31] L. Eren, T. Ince, and S. Kiranyaz, "A generic intelligent bearing fault diagnosis system using compact adaptive 1D CNN classifier," *Journal of Signal Processing Systems*, vol. 91, no. 2, pp. 179–189, 2019.

[32] J. Koutnik, K. Greff, F. Gomez, and J. Schmidhuber, "A clockwork RNN," in *International Conference on Machine Learning*, pp. 1863–1871, PMLR, 2014.

[33] S. Hochreiter and J. Schmidhuber, "Long short-term memory," *Neural computation*, vol. 9, no. 8, pp. 1735–1780, 1997.

[34] K. Cho, B. Van Merriënboer, C. Gulcehre, D. Bahdanau, F. Bougares, H. Schwenk, and Y. Bengio, "Learning phrase representations using RNN encoder-decoder for statistical machine translation," *arXiv preprint arXiv:1406.1078*, 2014.